

Numerical investigations of reactive pollutant dispersion and personal exposure in 3D urban-like models

Article

Accepted Version

Creative Commons: Attribution-Noncommercial-No Derivative Works 4.0

Zhang, Y., Yang, X., Yang, H., Zhang, K., Wang, X., Hang, J., Luo, Z. and Zhou, S. (2020) Numerical investigations of reactive pollutant dispersion and personal exposure in 3D urban-like models. Building and Environment, 169. 106569. ISSN 0360-1323 doi: <https://doi.org/10.1016/j.buildenv.2019.106569> Available at <https://centaur.reading.ac.uk/87490/>

It is advisable to refer to the publisher's version if you intend to cite from the work. See [Guidance on citing](#).

To link to this article DOI: <http://dx.doi.org/10.1016/j.buildenv.2019.106569>

Publisher: Elsevier

All outputs in CentAUR are protected by Intellectual Property Rights law, including copyright law. Copyright and IPR is retained by the creators or other copyright holders. Terms and conditions for use of this material are defined in the [End User Agreement](#).

www.reading.ac.uk/centaur

CentAUR

Central Archive at the University of Reading

Reading's research outputs online

To be submitted to Building and Environment 2019

Numerical investigations of reactive pollutant
dispersion and personal exposure in 3D urban-like models

**Yong Zhang¹, Xia Yang¹, Hongyu Yang¹, Keer Zhang¹, Xuemei Wang², Zhiwen
Luo³, Jian Hang^{1,4*}, Shengzhen Zhou^{1*}**

¹School of Atmospheric Sciences, Guangdong Province Key Laboratory for Climate
Change and Natural Disaster Studies, Sun Yat-sen University, Guangzhou, P.R. China

²Institute for Environmental and Climate Research, Jinan University, Guangzhou, P. R.
China

³School of the Built Environment, University of Reading, UK

⁴National Supercomputer center in Guangzhou, P.R. China

*Corresponding author: Jian Hang, Shengzhen Zhou

Tel: +86-13710248541; +86-13710952752

E-mail address: hangj3@mail.sysu.edu.cn; zhouszh3@mail.sysu.edu.cn

Abstract

With satisfactory validation by experimental data, we perform computational fluid dynamic(CFD) simulations with the standard $k-\varepsilon$ model to investigate how NO-NO₂-O₃ photochemistry and turbulent mixing influence reactive pollutant dispersion and vehicular NO_x exposure in 21-row(neighborhood-scale~1km) three-dimensional(3D) medium-dense urban models with an approaching wind parallel(perpendicular) to the main(secondary) streets. Personal intake fraction P_{iF} and its spatially-averaged values for the entire building (i.e. building intake fraction $\langle P_{iF} \rangle_B$) are adopted for reactive/passive exposure analysis with/without NO_x-O₃-photochemistry.

Some meaningful findings are proposed: 1) There are flow adjustment processes coupling turbulent mixing and chemical reactions through urban areas(i.e. secondary Street 1 to 20). NO-NO₂-O₃ photochemistry induces O₃ depletion and NO conversion into NO₂ producing significant increase in NO₂ exposure and slight decrease in NO exposure compared with passive dispersion. 2) With span-wise NO_x sources, Street 10 in the fully-developed region experiences weaker wind and subsequently greater $\langle P_{iF} \rangle_B$ (0.207ppm) than Street 3(0.135ppm) in the upstream flow-adjustment region. $\langle P_{iF} \rangle_B$ descends exponentially from the target building toward downstream, and Street 10 experiences quicker decay rates. 3) With stream-wise NO_x sources along the main street, $\langle P_{iF} \rangle_B$ first ascends, then reaches equilibrium values (e.g.0.046-0.049ppm for passive). 4) If background O₃ concentration [O₃] rises from 20ppbv to 40 and 100ppbv, more NO is oxidized by O₃ to generate NO₂. As [O₃]=20ppbv, if NO-NO₂ emission ratio decreases from 10 to 5, NO₂ exposure is

partly offset but NO exposure change little. Present methodologies are confirmed effective to investigate impacts of more complicated meteorological conditions and chemical mechanisms on exposure in urban districts.

Keywords: NO-NO₂-O₃ photochemistry; reactive pollutant dispersion; personal intake fraction (P_{iF}); building intake fraction ($\langle P_{iF} \rangle_B$); computational fluid dynamic (CFD) simulation; three-dimensional (3D) urban models

1. Introduction

Following the ongoing urbanization worldwide, vehicular pollutant emissions have become one of the major sources in urban air pollution[1-3]. Heavy traffic flows, compact urban configurations and unfavorable meteorological conditions are the main reasons of large pollutant exposure and adverse health impacts on city dwellers[4]. On average, people spend more than 90% of their time indoors. Outdoor air pollutants in urban areas can penetrate into indoor via doors, windows, building cracks and other ventilation duct systems[5-7]. Particularly, vehicular pollutant exposure to urban residents living near busy roads should be paid more attention, because they suffer from higher health risks than other urban microenvironments[7-10]. Apart from reducing vehicular pollutant emissions, sustainable urban design with better understanding the influence of urban layouts and atmospheric conditions on the flow and passive/reactive pollutant dispersion in urban areas can help enhancing pollutant

dilution and mitigating traffic-related pollutant exposure[11-15].

As reviewed by the literature[16-29], in the past decades, a number of computational fluid dynamic (CFD) simulations, outdoor field observations and wind tunnel experiments have been widely performed to clarify turbulent flow characteristics and pollutant dispersion in urban models from street-scale (~100m) to neighborhood-scale (~1km). Street aspect ratios (H/W) are reported as the most key urban parameters in two-dimensional (2D) street canyons[16-18, 25-26, 29-32]. Realistic urban districts are usually three-dimensional (3D) with pollutant exchange across street roofs and lateral/stream-wise urban boundaries. Generally, the building planar area index λ_p (i.e. the ratio between the planar area of buildings viewed from above and the total floor area) and the frontal area index λ_f (i.e. the ratio of the frontal area of buildings to the total floor area) are typical building packing density indexes and key parameters of 3D urban areas[33-38]. Moreover, other significant factors have been also verified, such as building height variations[38-40], ambient wind directions[40-41], elevated building design[42-44], tree planting[46-49] etc. In addition, thermal stratification and buoyancy forces induced by wall heating and solar shading also significantly influence or dominate the flow and pollutant dispersion if wind speed is relatively small and Richardson number is large[50-56].

Recently, several researches[7, 44, 57] introduce personal intake fraction (P_{iF}) to quantify street-scale pollutant exposure induced by vehicle emissions. In contrast to population intake fraction (IF) for a specific population[4, 58], P_{iF} is independent of population density and size which represents the fraction of pollutants inhaled

averagely by each person of a population to the total pollutant emissions. For example, 1ppm (part per million or 10^{-6}) means the inhalation of 1mg pollutants if 1kg pollutants being emitted. By performing CFD simulations validated by experimental data, [Hang et al.\[7\]](#) estimated spatial mean P_{iF} (i.e. $\langle P_{iF} \rangle \sim 1\text{-}5\text{ppm}$) of passive pollutant (i.e. CO) in shallow 2D street canyons ($H/W=0.5\text{-}1$). Later, $\langle P_{iF} \rangle$ in 3D urban district models were confirmed one order smaller ($\sim 0.1\text{ppm}$) than 2D models with similar aspect ratios ($H/W=0.5\text{-}1$)[\[41, 57\]](#).

Besides the dynamic dispersion of passive pollutants, there are chemical processes of reactive pollutants in urban streets, such as the $\text{NO}_x\text{-O}_3$ photochemistry [\[59-64\]](#), $\text{NO}_x\text{-O}_3\text{-VOCs}$ chemical mechanisms[\[65-69\]](#) etc. Among them, the impacts of different heating scenarios and building configurations on reactive dispersion are extensively investigated through LES or RANS approaches, such as various shading settings[\[61\]](#), wall heating scenarios[\[60, 62\]](#), aspect ratios[\[63\]](#) etc. However, most studies so far mainly examine reactive pollutant dispersion in 2D street canyons while investigations on reactive pollutant dispersion and the related exposure in 3D urban models are still rare. Therefore, this study incorporates $\text{NO-NO}_2\text{-O}_3$ chemistry into CFD simulations and numerically investigates reactive pollutant dispersion and exposure in urban models. As a start, the impacts of various ground-level source locations and reactant proportions ($\text{NO}:\text{NO}_2:\text{O}_3$) in 3D medium-dense urban models ($H/W=1$, $\lambda_p=\lambda_f=0.25$) are studied under neutral meteorological conditions.

The sketch of this paper is organized as follows: Section [2](#) introduces the indexes for pollutant dispersion and exposure. Section [3](#) illustrates model setups and all test

cases in CFD simulations. Section 4 presents the flow and pollutant dispersion validations by wind tunnel data. Section 5 shows results and discussions, and Section 6 draws the conclusions.

2. Indexes for pollutant dispersion and exposure

2.1 Personal intake fraction (P_{iF}) and building intake fraction ($\langle P_{iF} \rangle_B$)

Population intake fraction (IF) and personal intake fraction (P_{iF}) are effective indexes to quantify vehicular pollutant exposure in local streets or neighborhoods[41, 44, 57]. Both exposure indexes are defined as Eq. (1):

$$IF = \sum_i^N \sum_j^M P_i \times Br_{ij} \times \Delta t_{ij} \times Ce_j / \dot{m} \quad (1a)$$

$$P_{iF} = IF / \sum_j^M P_i \quad (1b)$$

where, N and M are the number of age groups and microenvironments, P_i represents the population size for the age group i , Br_{ij} (m^3/s) and Δt_{ij} (s) are the average breathing rate and the individual time spent for the i th age group in the j th microenvironment, Ce_j (kg/m^3) denotes pollutant concentration in microenvironment j and \dot{m} (kg) means total emissions released from vehicles. It is worth mentioning that P_{iF} is independent of pollutant release rates as well as population density and size, but can be influenced by building configurations, meteorological conditions and pollutant source settings etc.

According to the literature[4, 70-71], the population data are categorized into

three subgroups($N=3$, Fig. 1a): Children(21.2%), Adults(63.3%) and Elders(15.5%). Moreover, the time activity patterns for each subgroup are divided into four microenvironments($M=4$, Fig. 1b): indoors at home($j=1$), other indoor locations($j=2$), in or near vehicles($j=3$), and other outdoor locations($j=4$). Table 1 lists activity time patterns and breathing rates in each subgroup for indoors at home($j=1$). In this study, all present building models are supposed to residential type and only $j=1$ (indoors at home) is adopted to calculate P_{iF} [44, 57]. Especially, the area-averaged P_{iF} of the building wall surface is denoted as wall intake fraction($\langle P_{iF} \rangle_w$). The spatially-averaged P_{iF} of the entire building surfaces is represented as building intake fraction($\langle P_{iF} \rangle_B$), which means the fraction of total traffic emissions inhaled averagely by each person living in this roadside building.

2.2 Photostationary state defect (d_{ps} , unit: %)

Referring to previous researches[59-60], the photostationary state defect (d_{ps}) is an effective indicator to measure the departure degree from photochemical equilibrium and can be expressed in the following form:

$$d_{ps} = \left(\frac{k_I[\text{NO}][\text{O}_3]}{J_{\text{NO}_2}[\text{NO}_2]} - 1 \right) \times 100 \quad (2)$$

here, $k_I[\text{NO}][\text{O}_3]$ and $J_{\text{NO}_2}[\text{NO}_2]$ represent the depletion and generation rates of ozone. d_{ps} is positive value if ozone depletion rate greater than its formation rate, and vice versa. Especially, d_{ps} equals zero when chemical reactions reach equilibrium state.

149

150 3. CFD setups and case descriptions

151 3.1 Numerical approaches

152 With advances in computer technologies, CFD as a powerful modelling tool has
153 been widely employed to reproduce turbulent flow structure as well as to predict
154 pollutant dispersion and transport in urban districts. Though large eddy simulations
155 (LES) have been confirmed to be more accurate in predicting turbulence than
156 Reynolds-Averaged Navier-Stokes (RANS) models[27, 73-75], RANS approaches are
157 still extensively used, since LES models require expensive computational expenses
158 and have challenges in selecting sub-grid scale models and specifying appropriate
159 boundary conditions. Moreover, among the RANS models (e.g. various $k-\varepsilon$ and $k-\omega$
160 models), the standard $k-\varepsilon$ model shows good agreements with experimental data and
161 has been widely adopted[7-8, 37-38, 45, 57-58, 76-79], although it has limitations in
162 predicting turbulent kinetic energy in strong-wind regions. Therefore, by considering
163 model performance and computational loads, the standard $k-\varepsilon$ model is selected to
164 solve the steady-state isothermal flow field. The governing equations for the flow and
165 turbulent quantities implemented are as below[80]:

166 The mass continuity equation:

$$167 \quad \frac{\partial \bar{u}_j}{\partial x_j} = 0 \quad (3)$$

168 The momentum equation:

$$\overline{u_j} \frac{\partial \overline{u_i}}{\partial x_j} = -\frac{1}{\rho} \frac{\partial \overline{p}}{\partial x_i} + \frac{\partial}{\partial x_j} \left(\nu \frac{\partial \overline{u_i}}{\partial x_j} - \overline{u_i' u_j'} \right) \quad (4)$$

The transport equations of turbulent kinetic energy (k) and its dissipation rate (ε):

$$\overline{u_i} \frac{\partial k}{\partial x_i} = \frac{\partial}{\partial x_i} \left[\left(\nu + \frac{\nu_t}{\sigma_k} \right) \frac{\partial k}{\partial x_i} \right] + P_k - \varepsilon \quad (5)$$

$$\overline{u_i} \frac{\partial \varepsilon}{\partial x_i} = \frac{\partial}{\partial x_i} \left[\left(\nu + \frac{\nu_t}{\sigma_\varepsilon} \right) \frac{\partial \varepsilon}{\partial x_i} \right] + C_{\varepsilon 1} \frac{\varepsilon}{k} P_k - C_{\varepsilon 2} \frac{\varepsilon^2}{k} \quad (6)$$

where, $\overline{u_j}$ is mean velocity components ($\overline{u_j} = \overline{u}, \overline{v}, \overline{w}$ as $j=1, 2, 3$); ν and $\nu_t = C_\mu \frac{k^2}{\varepsilon}$

($C_\mu=0.09$) represent the kinematic viscosity and the eddy viscosity, respectively; the

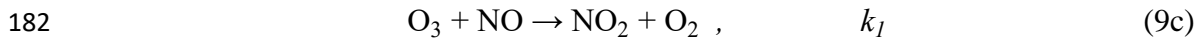
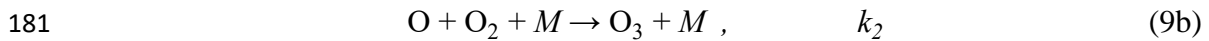
Reynolds stress tensor $-\overline{u_i' u_j'}$ and the turbulence production term P_k are defined as:

$$-\overline{u_i' u_j'} = \nu_t \left(\frac{\partial \overline{u_i}}{\partial x_j} + \frac{\partial \overline{u_j}}{\partial x_i} \right) - \frac{2}{3} k \delta_{ij} \quad (7)$$

$$P_k = \nu_t \times \frac{\partial \overline{u_i}}{\partial x_j} \left(\frac{\partial \overline{u_i}}{\partial x_j} + \frac{\partial \overline{u_j}}{\partial x_i} \right) \quad (8)$$

Note that δ_{ij} is the Kronecker delta whose value is 1 when $i=j$ and otherwise is 0.

The NO_x-O₃ simple photochemical mechanism is described as follows[59-60]:



Here, M denotes a third molecule, for example O₂ or N₂, to absorb excess energy and

stabilize O₃ molecule formed; J_{NO_2} , k_2 and k_1 represent rate constant for each

reaction, respectively. Since the oxygen atom (O) is highly reactive, it combines

rapidly with O₂ once O is produced from NO₂ photolysis. This is so-called

pseudo-steady-state approximation that the depletion and production rates of O₃ are

188 nearly equal[81]:

$$189 \quad k_2[\text{O}][\text{O}_2][\text{M}] = J_{\text{NO}_2}[\text{NO}_2] \quad (10)$$

190 Therefore, Eq. (9a) is the rate control step for O₃ formation. Based on the above
191 assumption, the transport equations for reactive pollutants can be defined as[59-60]:

$$192 \quad \bar{u}_j \frac{\partial [\text{NO}]}{\partial x_j} = D_m \frac{\partial^2 [\text{NO}]}{\partial x_j \partial x_j} + \frac{\partial}{\partial x_j} \left(D_e \frac{\partial [\text{NO}]}{\partial x_j} \right) + J_{\text{NO}_2}[\text{NO}_2] - k_I[\text{O}_3][\text{NO}] + S_{\text{NO}} \quad (11a)$$

$$193 \quad \bar{u}_j \frac{\partial [\text{NO}_2]}{\partial x_j} = D_m \frac{\partial^2 [\text{NO}_2]}{\partial x_j \partial x_j} + \frac{\partial}{\partial x_j} \left(D_e \frac{\partial [\text{NO}_2]}{\partial x_j} \right) - J_{\text{NO}_2}[\text{NO}_2] + k_I[\text{O}_3][\text{NO}] + S_{\text{NO}_2} \quad (11b)$$

$$194 \quad \bar{u}_j \frac{\partial [\text{O}_3]}{\partial x_j} = D_m \frac{\partial^2 [\text{O}_3]}{\partial x_j \partial x_j} + \frac{\partial}{\partial x_j} \left(D_e \frac{\partial [\text{O}_3]}{\partial x_j} \right) + J_{\text{NO}_2}[\text{NO}_2] - k_I[\text{O}_3][\text{NO}] \quad (11c)$$

195 where, D_m and D_e are the molecular and eddy diffusivity; the third terms on the
196 right-hand side of Eq. (11) represent chemical reaction term; S_{NO} and S_{NO_2} denote the
197 source terms of NO and NO₂; the Schmidt number $Sc_t = \nu_t / D_e$ is specified as 0.7[33, 39,
198 46, 48, 78]. Furthermore, the photolysis rate J_{NO_2} and rate constant k_I are calculated by
199 [59-60]:

$$200 \quad J_{\text{NO}_2} = 8.14 \times 10^{-3} \left\{ 0.97694 + 8.3700 \times 10^{-4} (T - 273.15) + 4.5173 \times 10^{-6} \times (T - 273.15)^2 \right\} \quad (12a)$$

201)

$$202 \quad k_I = 4.405 \times 10^{-2} \exp\left(-\frac{1370}{T}\right) \quad (12b)$$

203 Here, T is temperature in K; the units of J_{NO_2} and k_I are s⁻¹ and ppbv⁻¹s⁻¹.
204 Additionally, the temperature-dependent rate constant is not considered in isothermal
205 flow of this study, thus J_{NO_2} and k_I are 8.1×10^{-3} s⁻¹ and 4.450×10^{-4} ppbv⁻¹s⁻¹ by
206 assuming reactive pollutants undergo chemical processes under the isothermal
207 condition with a fixed T of 298.15K.

All governing equations(Eqs. (3-6, 11)) are discretized by a finite volume method (FVM) with the second-order upwind scheme. The SIMPLE algorithm is employed for pressure and velocity coupling. The under-relaxation factors for pressure, momentum, k and ε terms are specified as 0.3, 0.7, 0.8 and 0.8. Numerical simulation does not stop until the absolute residuals of all variables are less than 10^{-6} .

3.2 Three-dimensional (3D) urban model setups in CFD

The building layouts, as depicted in Fig. 2a, are based on the idealized 3D medium-dense urban clusters (i.e. street aspect ratio $H/W=1$; building packing density $\lambda_p=\lambda_f=0.25$). To better illustrate model configurations, x , y and z are described as the stream-wise, span-wise and vertical directions, respectively. The cubic building models($H=B=30\text{m}$) with a uniform spacing($W_s=W_m=30\text{m}$) are constructed in x and y directions. Moreover, the approaching wind is parallel to the main streets(x direction) and perpendicular to the secondary streets(y direction). $x/H=0$ means the cross section in windward street opening and $y/H=0$ denotes the central cross section of the main street (Fig. 2c).

As verified by the literature[38-40, 82-83], the airflow in the middle column is hardly affected by lateral boundaries if the lateral width of the urban model is sufficiently large. Hence, only half of the middle column with two lateral symmetry boundaries are considered during CFD simulations to reduce computational efforts (Fig. 2b). Following the CFD guidelines[84-86], the distances between urban

boundaries and the domain top, domain inlet, domain outlet are $9H$, $6.7H$ and $32.3H$, respectively. Furthermore, the zero normal gradient boundary condition is adopted at two lateral boundaries and the domain top (i.e. symmetry) and the domain outlet (i.e. outflow). Several recent studies[5-6, 8-9, 44, 57-58] reported that, pollutant concentration on the wall surfaces of near-road buildings can be treated as indoor concentration originated from outdoor pollutants since the indoor/outdoor (I/O) ratio of pollutant concentration is nearly one for naturally-ventilated buildings[5, 72]. Therefore, by assuming all present building models are naturally-ventilated type, the flow and pollutant dispersion within indoor space of buildings are not taken into account to reduce the grid numbers and computational costs in CFD simulations. The literature have applied such technique to effectively quantify vehicular pollutant exposure in 2D street canyons or 3D urban models[5-6, 8-9, 44, 57-58].

For the domain inlet, the power-law time-averaged velocity profile $U_0(z)$ in the upstream free flow is adopted (Eq. 13a)[40-41, 57, 82-83] which is scaled to that in wind tunnel experiments[87]. Base on the CFD guideline[84-86], vertical profiles of $k(z)$ and $\varepsilon(z)$ are given by Eqs. (13b-c):

$$U_0(z) = U_{ref} \times (z/H)^{0.16} \quad (13a)$$

$$k(z) = u_*^2 / \sqrt{C_\mu} \quad (13b)$$

$$\varepsilon(z) = C_\mu^{3/4} k^{3/2} / (\kappa_v z) \quad (13c)$$

where, U_{ref} is the reference velocity at the building height in upstream free flow ($U_{ref}=3.0$ m/s at $z = H$); the friction velocity $u_*=0.24$ m/s[40-41, 57, 82-83]; von

Karman constant $\kappa_v=0.41$, $C_\mu=0.09$. Furthermore, vertical profiles of Eq. (13) represent neutral atmospheric boundary layer with a full-scale surface roughness $z_0=0.1\text{m}$ [93] and have been adopted in previous studies[40-41, 57, 82-83].

In addition, Fig. 2c demonstrates the overhead and lateral views of mesh distribution for test cases. The minimum grid size of 0.2 m near the wall surfaces and the stretching ratio between adjacent grids of 1.15 (about 3.2 million hexahedral cells) are applied to ensure sufficiently fine grid at the pedestrian level (0-1.5m) and near building surfaces. As the normalized distance y^+ ($y^+=yu_\tau/\nu$) ranges from 30 to 600 at most regions of wall surfaces, standard wall function with no slip boundary condition is set on all wall surfaces. According to the literature[13, 40, 88-89], a specific roughness modification is assigned to the upstream and downstream ground to obtain a horizontally homogeneous ABL surrounding urban regions. Especially, the grid independence tests are presented later in subsection 4.1.

3.3 Pollutant source settings and model description of test cases

Three kinds of pollutant source locations are considered in this study, i.e. the span-wise (y direction) emission sources in the 3rd or 10th secondary street is denoted as S3 and S10 (Fig. 3a-b), and the stream-wise (x direction) emission sources along the main street is represented by Sm (Fig. 3c). The reactive pollutants involved in present photochemistry are NO, NO₂ and O₃. Among them, NO_x is assumed to be emitted from vehicles into the street canyon while background O₃ concentration is

specified at the domain inlet and entrained by approaching wind into urban districts. The background concentrations for NO and NO₂ at the domain inlet are zero in this study. Following the literature[59-60], typical automobile emission ratio of NO to NO₂ ($R_{\text{NO/NO}_2}$) of 10 is adopted. NO and NO₂ are released from the lowest grid cell ($z=0-0.2\text{m}$) at rates of 100 and 10 ppbv s⁻¹, which corresponds to emission strengths of 1.227×10^{-7} and 1.88×10^{-8} kg m⁻³s⁻¹ ($P=1$ atm, $T=298.15\text{K}$). For S3 or S10 sources, as the street width (W_s) is 30m, this NO_x emission intensity of 849 μg m⁻¹s⁻¹ is equivalent to a traffic volume of about 6100 vehicles per hour when considering a NO_x emission of 0.5g km⁻¹ per vehicle[59-60]. Particularly, we are mainly concerned with the proportion among NO and NO₂ rather than the assigned emission rate for each vehicular pollutant.

Furthermore, four O₃ background concentrations (i.e. [O₃] =1, 20, 40 and 100 ppbv) with $R_{\text{NO/NO}_2}=100:10$ are investigated to study the effects of different [O₃] on reactive dispersion. In addition, Carslaw[90] verified that there is an increasing NO₂/NO_x emission ratio in road traffic emissions referring to observation in real cities. Thus, three emission ratios of NO to NO₂ (i.e. $R_{\text{NO/NO}_2}=100:10$, 50:10 and 100:20) with [O₃]=20ppbv are considered to examine the impacts of various $R_{\text{NO/NO}_2}$ on reactive pollutant dispersion.

Overall, total 11 test cases are described as Case P [Source, $R_{\text{NO/NO}_2}$] or Case R [Source, $R_{\text{NO/NO}_2}$, [O₃]] and summarized in Table 2. Here ‘P’ means passive dispersion without chemical reactions, ‘R’ denotes reactive dispersion with NO-NO₂-O₃ chemistry; ‘Source’ contains three pollutant source locations, i.e. S3, S10 and Sm,

respectively; $R_{\text{NO/NO}_2}$ represents the emission ratios of NO to NO₂; $[\text{O}_3]$ is background O₃ concentration (mole fraction, unit: ppbv).

4 Validation study of flow and pollutant dispersion in 3D urban models

4.1 Flow validation by wind tunnel data

In this subsection, the performances of various steady k - ε models (standard, RNG and Realizable) with standard wall function are evaluated by wind tunnel data. Moreover, the grid independence tests are also implemented.

As shown in Fig. 4a-b, idealized 3D urban models in wind tunnel experiment[87] consist of 7 rows and 11 columns of regularly-aligned cubic buildings ($H=B=W=15\text{cm}$). Vertical profiles of velocity components (\bar{u} , \bar{w}) and turbulence kinetic energy (k) are measured at points of V_i ($i=1-6$), which are central positions in the i th secondary street located at $y/H=1$ and $x/H=1.5H, 3.5H, 5.5H, 7.5H, 9.5H, 11.5H$ respectively (Fig. 4a-b).

In CFD validation study, the similar full-scale model configurations ($H=B=W=30\text{m}$, Fig. 4c) are reconstructed with the scale ratio of 200:1 to wind-tunnel-scale models. Moreover, all CFD setups including computational domains, boundary conditions and convergence criteria in this full-scale CFD validation study are similar with those in subsection 3.2 except that the distance between urban boundaries and domain outlet is $40.3H$ (Fig. 4c). Based on the building height($H=0.15\text{m}$ or 30m) and reference velocity($U_{ref}=3\text{m/s}$), the reference Reynolds

314 number $Re = \frac{U_{ref}H}{\nu} \approx 30000$ and 6×10^6 for wind-tunnel-scale and full-scale urban
315 models, which are much larger than 11000 satisfying Reynolds number independence
316 requirement. Furthermore, Fig. 4d depicts the coarse, medium and fine grid
317 arrangements with hexahedral cells of about 1, 2 and 3.3 million and the minimum
318 grid size of 0.4m, 0.2m and 0.1m, respectively.

319 Fig. 5 first shows results of grid independence test at V1(Fig. 5a-b), then depicts
320 vertical profiles of time-averaged stream-wise velocity $\bar{u}(z)$ at Points V1, V4 and V6
321 (Fig. 5c-e), vertical velocity $\bar{w}(z)$ (Fig. 5f) and turbulence kinetic energy $k(z)$ (Fig. 5g)
322 at Point V1 between numerical results and experimental data. There is little difference
323 in numerical results between the coarse, medium and fine grid, and thus medium grid
324 is selected for case studies to reduce computational loads. Besides, the standard $k-\varepsilon$
325 model with the medium grid shows better agreements with wind tunnel data than the
326 RNG and Realizable $k-\varepsilon$ models.

327 To further quantify the modeling accuracy and reliability of the standard $k-\varepsilon$
328 model with the medium grid arrangement, several statistical performance metrics are
329 applied, including the mean value, the standard deviation, the factor 2 (FAC2), the
330 normalized mean square error (NMSE), the fraction bias (FB) and the correlation
331 coefficient (R)[91]. Among which, the closer NMSE value to zero, the smaller
332 difference between experiment data and CFD results; FAC2 value larger than one
333 means over-prediction against experiment data while smaller than one represents
334 under-prediction; Similarly, the negative and positive FB values denote
335 overestimation and underestimation. Results of $\bar{u}(z)$ at Points V1, V4 and V6 as well

as $\bar{w}(z)$ and $k(z)$ at Point V1 are listed in Table 3. Referring to COST Action 732's recommended criteria[91], a credible CFD model should satisfy the following statistical metrics standards: $0.5 \leq \text{FAC2} \leq 2$, $\text{NMSE} \leq 1.5$ and $-0.3 \leq \text{FB} \leq 0.3$. Overall, metrics lie in the recommended criteria, particularly values of $\bar{u}(z)$ meet well. However, values of $\bar{w}(z)$ and $k(z)$ reveal relatively poorer performance than those of $\bar{u}(z)$, which is largely attributed to the limitation of the standard $k-\varepsilon$ model. Conclusively, the validation study shows that present CFD methodologies applying standard $k-\varepsilon$ model with medium grid have credible numerical accuracy in predicting urban turbulent flow and can be employed for further case studies.

4.2 Validation of pollutant dispersion by wind tunnel data

Experimental and numerical studies have been extensively performed to investigate passive pollutant dispersion in the idealized street canyons. Unfortunately, there are currently little experimental data to directly validate the present CFD model coupled with chemistry[59-60, 63-64]. However, the reactive pollutants considered in this paper are effectively passive and can be divided into two subsets, i.e. total nitrogen oxide ($\text{NO}_x = \text{NO} + \text{NO}_2$) and total oxidant ($\text{OX} = \text{NO}_2 + \text{O}_3$), since reactions (Eq. 9) interconvert NO with NO_2 , and O_3 with NO_2 but without redundant productions. In addition, the chemical reaction terms cancel out when Eqs. (11a-b) and Eqs. (11b-c) are added, which indicates that the transport and dispersion of NO_x and OX can be deemed as passive scalar. Consequently, in this subsection, Standard $k-\varepsilon$ model with

standard wall function has been implemented and validated against wind tunnel experiment to evaluate the reliability of numerical simulation in predicting passive pollutant distribution.

The configurations of the wind tunnel measurement[92], as depicted in Fig.6a-b, are consisted of nine rectangular building models ($L_x=27.6\text{cm}$, $L_y=18.4\text{cm}$, $H=8\text{cm}$) with three rows and three columns (3×3) and uniform street widths ($W=8\text{cm}$, $H/W=1$). Moreover, tracer gas(C_2H_6) is released from a line source (0.5cm in width, dx and 18.4 cm in length, L_s) at a velocity of $w_{source}=0.01\text{ m/s}$ which is paralleled with y direction and locates in the central street canyon in front of building No.2(Fig. 6a-b). Furthermore, C_2H_6 concentration profiles are measured in the middle of leeward and windward walls near the line source as well as on the central line of roof surface in the building No.2(Fig. 6a-b).

In full-scale pollutant dispersion validation study, similar model configurations ($L_x=138\text{m}$, $L_y=92\text{m}$, $H=40\text{m}$, in Fig. 6c) are rebuilt with the scale ratio of 500:1 to wind-tunnel-scale models. CFD setups are similar with subsection 3.2, but the distances between urban boundaries and the domain top, domain side, domain inlet, domain outlet are $9H$, $5H$, $5H$ and $15H$, respectively. The approaching wind is parallel to the main streets(x direction) and perpendicular to the secondary streets(y direction). Furthermore, vertical profiles of stream-wise velocity $\bar{u}(z)$, turbulence kinetic energy $k(z)$ and turbulent dissipation rate $\varepsilon(z)$ fitted by measured data in wind tunnel experiments[92] are adopted at the domain inlet (Fig. 6d-f). In addition, to compare CFD results with measured data, the normalized C_2H_6 concentration K is defined as

below:

$$K=CHU_{ref}/w_{source}dx \quad (14)$$

Here the height of building (H), the reference velocity (U_{ref}) and the line source emission strength (w_{source}, dx) are applied.

As shown in Fig. 7, the agreements of K between wind tunnel data and CFD results are well confirming the standard $k-\varepsilon$ model has sufficient modeling accuracy in predicting passive pollutant dispersion within 3D urban district models.

5 Results and discussion

5.1 Flow patterns in 3D urban district models

Fig. 8a depicts velocity distribution in the plane of $z=1.5\text{m}$ (the pedestrian level). Obviously, the flow adjustment process can be observed through the entire building clusters, in which wind speed decreases toward downstream from Street 1 to Street 6, and then reaches a comparatively flow equilibrium from Street 7 to Street 18. Fig. 8b-c further depict velocity magnitude and 2D streamlines in the plane of $y=30\text{m}$ (the center plane of the target street canyon) and $z=1.5\text{m}$ for Street 3 and Street 10. Moreover, the corresponding 3D streamlines are displayed in Fig. 8d. For both street units, 3D downward helical vortices are produced inside the secondary streets (Fig. 8b-d). The lateral flow direction near street ground (i.e. $z=1.5\text{m}$) are from the secondary streets to the main streets and from the downwind building (No.4 and 11)

to upwind building (No. 3 and 10) (Fig. 8c). In addition, Street 3 apparently experiences greater wind speed than Street 10.

In particular, the following analysis (subsection 5.3) emphasizes more on reactive pollutant dispersion in the fully-developed region (e.g. Street 10) than the flow-adjust region (e.g. Street 3).

5.2 Impacts of source locations (S3, S10 and Sm) on reactive pollutant dispersion

This subsection considers the impacts of source locations (i.e. S3, S10 and Sm in Fig. 3) on reactive pollutant dispersion (with chemical reactions, R-type) under the specific pollutant proportion (i.e. $R_{\text{NO}/\text{NO}_2}=100:10$, $[\text{O}_3]=20\text{ppbv}$). Because the present photochemical mechanism contains the interconversion of nitrogen oxides (i.e. $\text{NO}_x=\text{NO}+\text{NO}_2$) and oxidants (i.e. $\text{OX}=\text{NO}_2+\text{O}_3$), The following discussions (subsection 5.2 and 5.3) concentrate more on NO_2 to simplify analysis. Moreover, passive dispersion (without chemical reactions, P-type) are also presented to investigate the sole role of turbulent mixing.

5.2.1 NO_2 concentration distribution in 3D urban-like models

Fig. 9a-d exhibit NO_2 concentration between P-type (passive, left) and R-type (reactive, right) cases in $y=30\text{m}$ and $z=1.5\text{m}$ for Street 3 and 10 fixed with span-wise sources (i.e. S3 and S10). Moreover, Fig. 9e compares NO_2 concentration at the

pedestrian level between passive and reactive cases with NO_x sources along main streets (i.e. Sm). For passive dispersion with S3 or S10 sources (P-type), due to source emissions and turbulent transports, NO_2 concentration near the upwind building (No.3 and 10) is higher than that near the downwind building(Fig. 9a-b). Furthermore, a large amount of NO_2 pollutants accumulate in the intersection of main street and secondary street(Fig. 9c-d). In an overall view, NO_2 concentration in Street 10 is slightly higher than Street 3. For P-type case with Sm sources(Fig. 9e), NO_2 concentration first rises toward downstream streets, then reaches an approximate equilibrium from Street 7 to 18. Such findings are similar with the flow adjustment as discussed in subsection 5.1.

With chemical reactions, as verified by Fig. 9, NO_2 concentration in R-type cases considerably exceeds that in P-type cases. Oppositely, passive NO concentration is higher than that in R-type cases.

5.2.2 d_{ps} distribution in Street 3 and 10

Fig. 10 shows d_{ps} distribution in $y=30\text{m}$ and $z=1.5\text{m}$ in local target streets with S3 and S10 sources. Here, the distribution of photostationary state defect(d_{ps}) is emphasized below the roof level ($z/H<1$) and toward downstream domains (i.e. $x/H>5$ and $x/H>19$ for Street 3 and 10, respectively).

As introduced in subsection 2.2, smaller d_{ps} value represents the less departure degree from photochemical equilibrium. In the centre plane of secondary streets

($y=30\text{m}$, Fig. 10a), the local small d_{ps} values emerge near the roof of the upwind building (No.3 and 10) while the large d_{ps} values appear near the roof of the downwind building (No.4 and 11) and the ground level close to NO_x emissions. At the pedestrian level(Fig. 10b), downstream areas of the main streets ($x/H>6$ and $x/H>20$) experience small d_{ps} values while the junction regions of the main street and secondary street near NO_x source locations obtain large d_{ps} values, particularly in Street 3. In summary, d_{ps} value is usually smaller in regions with weaker wind and turbulence, where reactive pollutants have more time to mix and react.

5.2.3 Concentration, $\langle P_{iF} \rangle_w$ and $\langle P_{iF} \rangle_B$ on building wall surfaces

Based on spatial mean concentration at the entire building surfaces, we calculate wall intake fraction($\langle P_{iF} \rangle_w$) and building intake fraction($\langle P_{iF} \rangle_B$) to analyze overall vehicular pollutant(NO_x) exposure in near-road buildings. Especially, 1ppm represents 1 mg inhaled averagely by each person living in the near-road building if 1kg pollutants emitted out.

Fig. 11a-b first compare NO_2 concentration on the leeward and windward walls between P-type and R-type cases in target street units with S3 and S10 sources. No matter with or without chemical reactions, NO_2 concentrations on the leeward wall are always higher than those on the windward wall. Once $\text{NO}_x\text{-O}_3$ photochemical reactions are conducted, an increase of NO_2 concentration emerges on the upwind and downwind walls. Such results are similar with the aforementioned discussion in

subsection 5.2.1.

Then, Table 4 lists $\langle P_{iF} \rangle_w$ of NO and NO₂ at leeward and windward walls adjoining target street in cases with S3 and S10 (positions as described in Fig. 3a-b). Obviously, in both P-type and R-type cases, $\langle P_{iF} \rangle_w$ of NO_x at leeward wall (Table 4, row 1-4, column 2-3) are greater than those at windward wall (Table 4, row 1-4, column 4-5). Regarding P-type cases as the references, $\langle P_{iF} \rangle_w$ of NO₂ in R-type cases rise nearly 90%-160%, i.e. 0.660 to 1.372ppm and 0.853 to 1.643ppm at leeward wall for S3 and S10 (Table 4, column 2), 0.180 to 0.473ppm and 0.230 to 0.610ppm at windward wall for S3 and S10 (Table 4, column 4); while $\langle P_{iF} \rangle_w$ of NO reduces about 9%-16%, i.e. 0.660 to 0.588ppm and 0.853 to 0.775ppm at leeward wall for S3 and S10 (Table 4, column 3), 0.180 to 0.151ppm and 0.230 to 0.193ppm at windward wall for S3 and S10 (Table 4, column 5). Because NO_x emission ratio released from vehicles is $R_{NO/NO_2}=10$, the present photochemical processes lead to a significant increase in NO₂ exposure and a slight decrease in NO exposure.

Furthermore, NO₂ concentrations on the entire building wall surfaces with Sm sources are presented in Fig. 11c. Both P-type and R-type cases experience the NO₂ concentration adjustment processes toward downstream buildings. To quantify NO_x exposure adjustments in P-type and R-type cases with various sources (S3, S10 and Sm), the horizontal profiles of building intake fraction $\langle P_{iF} \rangle_B$ of NO and NO₂ are shown in Fig. 12. It is found that $\langle P_{iF} \rangle_B$ with S3 or S10 sources descends exponentially toward downstream buildings (Fig. 12a-b), instead, $\langle P_{iF} \rangle_B$ with Sm sources first ascends quickly from building No.1 to 8, then reaches an approximate

equilibrium(Fig. 12c). Besides, R-type cases experience larger NO₂ exposure than P-type cases, i.e. 0.420-0.108ppm against 0.135-0.020ppm for S3(Fig. 12a), 0.605-0.160ppm against 0.207-0.030ppm for S10(Fig. 12b), 0.005-0.090ppm against 0.002-0.049ppm for Sm(Fig. 12c). Oppositely, NO exposure in P-type cases are greater than R-type cases, i.e. 0.135-0.020ppm than 0.106-0.010ppm for S3(Fig. 12a), 0.207-0.030ppm than 0.168-0.017ppm for S10(Fig. 12b) and 0.002-0.049ppm than 0.002-0.045ppm for Sm(Fig. 12c).

In addition, the decay function expressed in $\langle P_{iF_n} \rangle_B = a \times \langle P_{iF_t} \rangle_B \times e^{(t-n)/b}$ is employed to further quantify the $\langle P_{iF} \rangle_B$ decay processes from target building unit ($t=4$ or 11) toward downstream building ($n=t$ to 21) in S3 and S10 cases. Note that, smaller decay factor b means relatively sharper descending processes of $\langle P_{iF} \rangle_B$ curves. Table 5 summarizes the $\langle P_{iF_t} \rangle_B$ of building “No. t ” and the exponential decay factors b in S3 and S10 cases. Obviously, compared with those in P-type case ($b=7.46$ and 3.96 in Table 5, row 1 and 3), R-type cases with S3 and S10 obtain larger b for NO₂ (10.80 and 6.84 in Table 5, row 2 and 4) and smaller b for NO (5.92 and 2.91). Moreover, $\langle P_{iF} \rangle_B$ curves in S10 cases(Table 5, row 3-4) decline more sharply toward downstream regions than S3 cases(Table 5, row 1-2). Particularly, as shown in Fig. 12c, $\langle P_{iF_t} \rangle_B$ in Sm cases are calculated by the mean $\langle P_{iF} \rangle_B$ from building No.9 to 21, i.e. 0.048ppm in P-type case, 0.044ppm and 0.088ppm in R-type case for NO and NO₂.

In summary, with $R_{\text{NO/NO}_2}=100:10$ and $[\text{O}_3]=20\text{ppbv}$, the present NO_x-O₃ titration interactions result in the production of NO₂ and depletion of O₃ and NO. By

focusing on $\langle P_{iF} \rangle_B$ values, NO₂ exposure in R-type cases are greater than P-type cases about 3.1 times for S3, 2.9 times for S10 and 1.8 times for Sm while NO exposure in R-type cases are nearly 21%, 19% and 8% smaller than P-type cases for S3, S10 and Sm, respectively.

5.3 Impacts of reactant proportions (NO:NO₂:O₃) on reactive pollutant dispersion

In this subsection, based on S10 sources, we discuss the effects of different reactant proportions (NO:NO₂:O₃) on the interaction of turbulent mixing and photochemical processes in urban districts. Additionally, P_{iF} and $\langle P_{iF} \rangle$ are independent on source emission strength in passive pollutant dispersion, therefore Case P[S10,100:10] is treated as the reference case to compare with the cases with other reactant proportions.

5.3.1 Impacts of O₃ background concentration ([O₃])

With the same emission ratio of NO to NO₂ (i.e. $R_{NO/NO_2}=100:10$), the impacts of four O₃ background concentrations (i.e. [O₃] = 1, 20, 40 and 100ppbv) on reactive pollutant dispersion are examined.

It is apparent that the formation of NO by photolyzing NO₂ is slightly dominant in photochemistry when [O₃] is 1ppbv. In contrast to the reference values (0.853 and 0.230ppm in [Table 4, row 3](#)), $\langle P_{iF} \rangle_w$ of NO₂ at the leeward and windward walls

slightly decrease(i.e. 0.816 and 0.211ppm in Table 4, row 5) while $\langle P_{iF} \rangle_w$ of NO increase a little(i.e. 0.858 and 0.233ppm). Besides, such phenomenon is distinctly observed in $\langle P_{iF} \rangle_B$ curves(Fig. 13) between the reference case and Case R [S10,100:10,1], i.e. 0.207-0.030ppm against 0.187-0.020ppm for NO₂(Fig. 13a) and 0.207-0.030ppm against 0.209-0.031ppm for NO(Fig. 13b).

However, if [O₃] rises from 20ppbv to 40 and 100ppbv, more NO is oxidized by O₃ to generate NO₂. Based on the reference values (0.853 and 0.230ppm in Table 4, row 3), $\langle P_{iF} \rangle_w$ of NO₂ become about 1.9-5.2 times greater (1.643, 2.454 and 4.442ppm in Table 4, column 2) at leeward wall and 2.6-6.7 times larger (0.610, 0.944 and 1.534ppm in Table 4, column 4) at windward wall; while $\langle P_{iF} \rangle_w$ of NO reduces approximately 9%-42% (0.775, 0.694 and 0.495ppm in Table 4, column 3) at leeward wall and 16%-57% (0.193, 0.159 and 0.100ppm in Table 4, column 5) at windward wall. Furthermore, Fig. 13 and Table 5 display the corresponding $\langle P_{iF} \rangle_B$ curves, $\langle P_{iF} \rangle_B$ values and decay factors b under different [O₃]. As depicted in Fig. 13, compared with Case R[S10,100:10,20], Case R[S10,100:10,100] and R[S10,100:10,40] obviously attain much larger $\langle P_{iF} \rangle_B$ of NO₂ (1.573-0.275 and 0.952-0.218ppm in Fig. 13a) and smaller $\langle P_{iF} \rangle_B$ of NO (0.071-0.005 and 0.133-0.011ppm in Fig. 13b). Additionally, both decay factors of NO₂ and NO are smaller ($b=6.02$ and 2.33 for [O₃]=40ppbv, $b=4.74$ and 1.87 for [O₃]=100ppbv in Table 5, row 6-7) than those in Case R[S10,100:10,20] ($b=6.84$ and 2.91 in Table 5, row 4), which implies higher [O₃] induces the quicker decay of $\langle P_{iF} \rangle_B$ curves for NO_x with S10 sources toward downstream building units. By concentrating on

$\langle P_{iF} \rangle_B$, NO₂ exposure in R-type cases surpass the reference case nearly 2.9, 4.6 and 7.6 times for [O₃]=20, 40 and 100ppbv, respectively (Table 5, column 2). Correspondingly, $\langle P_{iF} \rangle_B$ of NO in these [O₃] cases are about 19%, 36% and 66% smaller than the reference values, respectively (Table 5, column 4). It clearly indicates that increasing [O₃] would aggravate NO₂ exposure within urban clusters but is conducive to the mitigation of NO exposure.

5.3.2 Effects of emission ratio of NO to NO₂ (R_{NO/NO_2})

The effects of source emission ratios (R_{NO/NO_2} =100:10, 50:10 and 100:20) on reactive pollutant dispersion are investigated with the same [O₃] of 20ppbv.

It is shown that decreasing NO or increasing NO₂ emissions based on the reference case can mildly change the fraction of NO converting into NO₂. For example, reducing R_{NO/NO_2} from 100:10 to 50:10 and 100:20, $\langle P_{iF} \rangle_W$ of NO varies from 0.775 to 0.744 and 0.784ppm at the leeward wall (Table 4, column 3), and from 0.193 to 0.186 and 0.197ppm at windward wall (Table 4, column 5). Furthermore, $\langle P_{iF} \rangle_W$ of NO₂ drops from 1.643 to 1.406 and 1.205ppm at the leeward wall (Table 4, column 1), and from 0.610 to 0.453 and 0.400ppm at windward wall (Table 4, column 4). In addition, Fig. 14 presents $\langle P_{iF} \rangle_B$ curves of NO₂ and NO in P-type and R-type cases with three NO-NO₂ emission ratios. Obviously, photochemical reactions in these R-type cases are still dominated by the depletion of O₃ with NO to produce NO₂.

As displayed in Fig. 14a and Table 5, Case R[S10,50:10,20] and R[S10,100:20,20] obtain smaller $\langle P_{iF} \rangle_B$ and decay factor of NO₂ (i.e. 0.446-0.091 ppm, $b=5.41$ and 0.384-0.088ppm, $b=6.00$) than those in Case R[S10,100:10,20] (i.e. 0.605-0.160ppm, $b=6.84$). In contrast to Case R[S10,100:10,20], $\langle P_{iF} \rangle_B$ of NO in Case R[S10,50:10,20] and R[S10,100:20,20] reduce nearly 26% and 37%. However, $\langle P_{iF} \rangle_B$ curves and decay factors b of NO are quite close between three R-type cases, i.e. 0.172-0.018, 0.168-0.018 and 0.160-0.017ppm; $b=3.05$, 2.91 and 3.11(Fig. 14b and Table 5). It is confirmed that the decrement of R_{NO/NO_2} (from 10 to 5) can partly offset NO₂ exposure but have much less impacts on NO exposure.

Overall, the NO_x-O₃ photochemical processes dependent on the initial proportion of reactive pollutants are toward satisfying the photostationary state relationship (i.e. $k_I[NO][O_3]=J_{NO_2}[NO_2]$).

5.4 Limitations and future work

Since the 3D urban district models, photochemical reactions and meteorological conditions adopted in this study are fairly simplified, the present exposure results may change if more realistic factors are taken into account, such as more realistic urban configurations(e.g. with variations of building height and street width), more complicated chemical mechanisms(e.g. VOCs-NO_x-O₃) and more realistic atmospheric conditions etc. It is worth mentioning that the chemical processes dependent on reaction rates are highly associated with the reactive pollutant

concentration and ambient air temperature. Moreover, realistic atmospheric conditions include the unsteady temporal and spatial variations of wind speed and direction as well as various atmospheric stabilities and solar radiation conditions. Thus, further unsteady CFD simulations will be performed to examine the integrated impacts of urban turbulence and solar radiation on reactive pollutant dispersion in 3D urban districts.

6 Conclusions

Urban residents in near-road buildings commonly suffer from high exposure risk of vehicular pollutants in which NO_x (NO and NO_2) act as primary reactive pollutants. With satisfactory full-scale CFD validation of flow and pollutant dispersion by experimental data, this study first focuses on the impact of turbulent transport combined with NO_x - O_3 photochemical reactions on reactive pollutant dispersion in neighborhood-scale (21-row, $\sim 1\text{km}$) three-dimensional (3D) medium-dense urban clusters ($H/W=1$, $\lambda_p=\lambda_f=0.25$). Ground-level emission sources of NO and NO_2 are considered in the presence of background O_3 . The approaching wind is parallel to the main streets and perpendicular to the secondary streets. As a start, the influences of various source locations and reactant proportions ($\text{NO}:\text{NO}_2:\text{O}_3$) on pollutant dispersion are investigated under neutral meteorological condition. Personal intake fraction P_{iF} , its spatially-averaged values for a building wall ($\langle P_{iF} \rangle_w$) and the entire building surfaces (i.e. building intake fraction $\langle P_{iF} \rangle_B$) are adopted to quantify pollutant

exposure with and without NO-NO₂-O₃ reactions(i.e. reactive and passive).

Some meaningful findings are summarized as below:

1) There are flow adjustment processes coupling turbulent mixing and chemical reactions through urban building clusters(Street 1 to Street 20 toward downstream).With span-wise sources, the secondary street of Street 10 located in the fully-developed region(i.e. S10 case) experiences weaker wind and subsequently greater $\langle P_{iF} \rangle_B$ than the secondary Street 3 located in the upstream flow-adjustment region (i.e. S3 case). Consequently, in contrast to S3 case, photostationary state defect (d_{ps}) is smaller in S10 case since reactive pollutants have more time to mix and react in Street 10.

2) With source emission ratios of NO to NO₂ of 10($R_{NO/NO_2}=100:10$) and background O₃ concentration of 20ppbv([O₃]=20ppbv), NO-NO₂-O₃ photochemistry leads to production of NO₂ and depletion of O₃ and NO, inducing a significant increase in NO₂ exposure and a slight decrease in NO exposure when compared to corresponding passive dispersion which only considers the sole role of turbulent transport. With span-wise pollutant sources, 3D downward helical flows transport more NO_x to the leeward side, inducing much greater leeward-side $\langle P_{iF} \rangle_w$ than the windward-side. Moreover, by defining exponential decay function expressed in $\langle P_{iF}_n \rangle_B = a \times \langle P_{iF}_t \rangle_B \times e^{(t-n)/b}$, it is found that $\langle P_{iF} \rangle_B$ descends exponentially from target building ($\langle P_{iF} \rangle_B=0.135\text{ppm}$ or 0.207ppm , $t=4$ or 11 for S3 or S10) to downstream buildings ($n=t$ to 21). Especially, $\langle P_{iF} \rangle_B$ curves decline more sharply

631 from Street 10 toward downstream than that from Street 3. However, if stream-wise
632 sources fixed along the main streets, $\langle P_{iF} \rangle_B$ first ascends quickly from building
633 No.1 to 8, then reaches approximate equilibrium values of $\langle P_{iF} \rangle_B =$
634 0.046-0.049ppm.

635 3) Furthermore, the O_3 background concentration ($[O_3]$) and source emission
636 ratios of NO to NO_2 (R_{NO/NO_2}) are confirmed as key factors on NO_x - O_3 reactive
637 dispersion. The formation of NO by photolyzing NO_2 is slightly dominant in
638 photochemistry when $[O_3]$ is 1ppbv. However, if $[O_3]$ rises from 20ppbv to 40 and
639 100ppbv, more NO is oxidized by O_3 to generate NO_2 , which would aggravate NO_2
640 exposure within urban clusters but is conducive to the mitigation of NO exposure.
641 Under $[O_3]$ of 20ppbv, results show that the decrement of R_{NO/NO_2} from 10 to 5 can
642 partly offset NO_2 exposure but have much less impacts on NO exposure.

643 Although further investigations are still required to provide practical guidelines,
644 this paper is one of the first attempts to quantify how reactive pollutant source
645 locations and reactant proportions influence reactive pollutant exposure in 3D urban
646 districts, which can present meaningful references for urban planning. The effective
647 methodologies are proposed for reactive pollutant exposure assessment in more
648 complicated urban districts with various meteorological conditions and chemical
649 mechanisms.

651 Acknowledgements

This study was financially supported by National Key R&D Program of China [2016YFC0202206, 2016YFC0202205 and 2016YFC0202204], the National Science Fund for Distinguished Young Scholars (No. 41425020) and National Natural Science Foundation--Outstanding Youth Foundation (No. 41622502), STINT (dnr CH2017-7271) and the National Natural Science Foundation of China (No. 51811530017 and 41875015).

References list

- [1] Fengler, J., 1999. Urban air quality. *Atmos. Environ.* 33(29): 4877-4900.
- [2] Chan, C.K., Yao, X.H., 2008. Air pollution in mega cities in China. *Atmos. Environ.* 42: 1-42.
- [3] Pu, Y.C., Yang, C., 2014. Estimating urban roadside emissions with an atmospheric dispersion model based on in-field measurements. *Environ. Pollut.* 192: 300-307.
- [4] Luo, Z.W., Li, Y.G., Nazaroff, W.W., 2010. Intake fraction of nonreactive motor vehicle exhaust in Hong Kong. *Atmos. Environ.* 44: 1913-1918.
- [5] Chen, C., Zhao, B., Zhou, W.T., Jiang, X.Y., Tan, Z.C., 2012. A methodology for predicting particle penetration factor through cracks of windows and doors for actual engineering application. *Build. Environ.* 47: 339-348.

- 671 [6] Ji, W.J., Zhao, B., 2015. Estimating mortality derived from indoor exposure to
672 particles of outdoor origin. *PLOS.ONE*.10, 0124238.
- 673 [7] Hang, J., Luo, Z.W., Wang, X.M., He, L.J., Wang, B.M., Zhu, W., 2017. The
674 influence of street layouts and viaduct settings on daily CO exposure and intake
675 fraction in idealized urban canyons. *Environ. Pollut.* 220: 72-86.
- 676 [8] Ng, W., Chau, C., 2014. A modeling investigation of the impact of street and
677 building configurations on personal air pollutant exposure in isolated deep urban
678 canyons. *Sci. Total Environ.* 468-469: 429-448.
- 679 [9] He, L.J., Hang, J., Wang X.M., Lin B.R., Li, X.H., Lan, G.D., 2017. Numerical
680 investigations of flow and passive pollutant exposure in high-rise deep street
681 canyons with various street aspect ratios and viaduct settings. *Sci. Total Environ.*
682 584-585: 189-206.
- 683 [10] Scungio, M., Stabile, L., Rizza, V., Pacitto, A., Russi, A., Buonanno, G., 2018.
684 Lung cancer risk assessment due to traffic-generated particles exposure in urban
685 street canyons: A numerical modelling approach. *Sci. Total. Environ.* 631-632:
686 1109-1116.
- 687 [11] Gu, Z.L., Zhang, Y.W., Cheng, Y., Lee, S.C., 2011. Effect of uneven building
688 layout on air flow and pollutant dispersion in non-uniform street canyons. *Build.*
689 *Environ.* 46: 2657-2665.
- 690 [12] Yuan, C., Ng, E., 2012. Building porosity for better urban ventilation in
691 high-density cities - A computational parametric study. *Build. Environ.* 50:

692 176-189.

693 [13]Blocken, B., Vervoort, R., van Hooff, T.A.J., 2016. Reduction of outdoor
694 particulate matter concentrations by local removal in semi-enclosed parking
695 garages: a preliminary case study for Eindhoven city center. *J. Wind Eng. Ind.*
696 *Aerodyn.* 159: 80-98.

697 [14]Santiago, J.L., Borge, R., Martin, F., de la Paz, D., Martilli, A., Lumbreras, J.,
698 Sanchez, B., 2017. Evaluation of a CFD-based approach to estimate pollutant
699 distribution within a real urban canopy by means of passive samplers. *Sci. Total*
700 *Environ.* 576: 46-58.

701 [15]Wang, W.W., Xu, Y., Ng, E., Raasch, S., 2018. Evaluation of satellite-derived
702 building height extraction by CFD simulations: A case study of
703 neighborhood-scale ventilation in Hong Kong. *Landscape. Urban. Plan.* 170:
704 90-102.

705 [16]Oke, T.R., 1988. Street design and urban canopy layer climate. *Energ. Buildings.*
706 11: 103-113.

707 [17]Vardoulakis, S., Fisher, B.E.A., Pericleous, K., Gonzalez-Flesca, N., 2003.
708 Modelling air quality in street canyons: a review. *Atmos. Environ.* 37: 155-182.

709 [18]Fernando, H.J.S., Zajic, D., Di Sabatino, S., Dimitrova, R., Hedquist, B., 2010.
710 Flow, turbulence, and pollutant dispersion in urban atmospheres. *Phys. Fluids.* 22:
711 1-20.

- 712 [19]Britter, R.E., Hanna, S.R., 2003. Flow and dispersion in urban areas. *Annu. Rev.*
713 *Fluid. Mech.* 35: 469-496.
- 714 [20]Di Sabatino, S., Buccolieri, R., Salizzoni, P., 2013. Recent advancements in
715 numerical modelling of flow and dispersion in urban area: a short review. *Int. J.*
716 *Environ. Pollut.* 52: 172-191.
- 717 [21]Blocken, B., 2015. Computational fluid dynamics for urban physics: importance,
718 scales, possibilities, limitations and ten tips and tricks towards accurate and
719 reliable simulations. *Build. Environ.* 91: 219-245.
- 720 [22]Srebric, J., Heidarinejad, M., Liu, J.Y., 2015. Building neighborhood emerging
721 properties and their impacts on multi-scale modeling of building energy and
722 airflows. *Build. Environ.* 91: 246-262.
- 723 [23]Meroney, R.N., 2016.Ten questions concerning hybrid computational/physical
724 model simulation of wind flow in the built environment. *Build. Environ.* 96:
725 12-21.
- 726 [24]Toparlar, Y., Blocken, B., Maiheu, B., van Heijst, G.J.F., 2017. A review on the
727 CFD analysis of urban microclimate. *Renew. Sustain. Energy Rev.* 80:
728 1613-1640.
- 729 [25]Zhong, J., Cai, X.M., Bloss, W.J., 2016. Coupling dynamics and chemistry in the
730 air pollution modelling of street canyons: A review. *Environ. Pollut.* 214:
731 690-704

- 732 [26]Zhang Y.W., Gu Z., Chuck W. Y., 2018. Review on numerical simulation of
733 airflow and pollutant dispersion in urban street canyons under natural background
734 wind conditions. *Aerosol. Air. Qual. Res.* 18: 780-789.
- 735 [27]Blocken, B., 2018. LES over RANS in building simulation for outdoor and
736 indoor applications : A foregone conclusion ? *Build. Simul.* 821-870.
- 737 [28]Lai, D., Liu, W., Gan, T., Liu, K., Chen, Q., 2019. A review of mitigating
738 strategies to improve the thermal environment and thermal comfort in urban
739 outdoor spaces. *Sci. Total Environ.* 661: 337-353.
- 740 [29]Li, X., Liu, C.H., Leung, D.Y.C., Lam, K.M., 2006. Recent progress in CFD
741 modelling of wind field and pollutant transport in street canyons. *Atmos. Environ.*
742 40: 5640-5658.
- 743 [30]Li, X.X., Liu, C.H., Leung, D.Y.C., 2009. Numerical investigation of pollutant
744 transport characteristics inside deep urban street canyons. *Atmos. Environ.* 43
745 (15): 2410-2418.
- 746 [31]Lin, L., Hang, J., Wang, X.X., Wang, X.M., Fan, S.J., Fan, Q., Liu, Y.H., 2016.
747 Integrated effects of street layouts and wall heating on vehicular pollutant
748 dispersion and their reentry into downstream canyons. *Aerosol Air Qual. Res.* 16:
749 3142-3163.
- 750 [32]Ding, S., Huang, Y.D., Cui, P.Y., Wu, J., Li, M.Z., Liu, D.T., 2019. Impact of
751 viaduct on flow reversion and pollutant dispersion in 2D urban street canyon with

752 different roof shapes -Numerical simulation and wind tunnel experiment. Sci.
753 Total. Environ. 671: 976-991.

754 [33]Chang, C.H., Meroney, R.N., 2003. Concentration and flow distributions in urban
755 street canyons: wind tunnel and computational data. J. Wind Eng. Ind. Aerodyn.
756 91: 1141-1154.

757 [34]Buccolieri, R., Sandberg, M., Di Sabatino, S., 2010. City breathability and its link
758 to pollutant concentration distribution within urban-like geometries. Atmos.
759 Environ. 44: 1894-1903.

760 [35]Hang, J., Li, Y.G., 2011. Age of air and air exchange efficiency in high-rise urban
761 areas. Atmos. Environ. 45 (31): 5572-5585.

762 [36]Yuan, C., Ng, E., Norford, L.K., 2014. Improving air quality in high-density cities
763 by understanding the relationship between air pollutant dispersion and urban
764 morphologies. Build. Environ. 71: 245-258.

765 [37]Ramponi, R., Blocken, B., de Coo, L.B., Janssen, W.D., 2015. CFD simulation of
766 outdoor ventilation of generic urban configurations with different urban densities
767 and equal and unequal street widths. Build. Environ. 92: 152-166.

768 [38]Chen, L., Hang, J., Sandberg, M., Claesson, L., Di Sabatino, S., Wigo, H., 2017.
769 The impacts of building height variations and building packing densities on flow
770 adjustment and city breathability in idealized urban models. Build. Environ. 118:
771 344-361.

- 772 [39]Hang, J., Li, Y.G., Sandberg, M., Buccolieri, R., Di Sabatino, S., 2012. The
773 influence of building height variability on pollutant dispersion and pedestrian
774 ventilation in idealized high-rise urban areas. *Build. Environ.* 56: 346-360.
- 775 [40]Lin, M., Hang, J., Li, Y., Luo, Z., Sandberg, M., 2014. Quantitative ventilation
776 assessments of idealized urban canopy layers with various urban layouts and the
777 same building packing density. *Build. Environ.* 79: 152-167.
- 778 [41]Sha, C.Y., Wang, X.M., Lin, Y.Y., Fan, Y.F., Chen, X., Hang, J., 2018. The
779 impact of urban open space and 'lift-up' building design on building intake
780 fraction and daily pollutant exposure in idealized urban models. *Sci. Total.*
781 *Environ.* 633: 1314-1328.
- 782 [42]Liu, J.L., Niu, J.L., Mak, C.M., Xia, Q., 2017. Detached eddy simulation of
783 pedestrian-level wind and gust around an elevated building. *Build. Environ.* 125:
784 168-179.
- 785 [43]Du, Y.X., Mak, C.M., Liu, J.L., Xia, Q., Niu, J.L., Kwok, K.C.S., 2017. Effects
786 of lift-up design on pedestrian level wind comfort in different building
787 configurations under three wind directions. *Build. Environ.* 117: 84-99.
- 788 [44]Zhang, K., Chen, G., Wang, X., Liu, S., Mak, C. M., Fan, Y., Hang, J., 2019.
789 Numerical evaluations of urban design technique to reduce vehicular personal
790 intake fraction in deep street canyons. *Sci. Total. Environ.* 653: 968-994.

- 791 [45]Chew, L.W., Nazarian, N., Norford, L., 2017. Pedestrian-level urban wind flow
792 enhancement with wind catchers. *Atmos.* 8(9): 159 (DOI: 10.3390/
793 atmos8090159)
- 794 [46]Buccolieri, R., Salim, S.M., Leo, L.S., Di Sabatino, S., Chan, A., Ielpo, P., de
795 Gennaro, G., Gromke, C., 2011. Analysis of local scale tree-atmosphere
796 interaction on pollutant concentration in idealized street canyons and application
797 to a real urban junction. *Atmos. Environ.* 45: 1702-1713.
- 798 [47]Buccolieri, R., Santiago, J.L., Rivas, E., Sanchez, B., 2018. Review on urban tree
799 modelling in CFD simulations: Aerodynamic, deposition and thermal effects.
800 *Urban for Urban Gree*, 31: 212-220.
- 801 [48]Gromke, C., Blocken, B., 2015. Influence of avenue-trees on air quality at the
802 urban neighborhood scale. Part I: quality assurance studies and turbulent Schmidt
803 number analysis for RANS CFD simulations. *Environ. Pollut.* 196: 214-223.
- 804 [49]Yuan, C., Norford, L., Ng, E., 2017. A semi-empirical model for the effect of
805 trees on the urban wind environment. *Landscape. Urban. Plan.* 168: 84-93.
- 806 [50]Xie, X.X., Huang, Z., Wang, J.S., 2006. The impact of urban street layout on
807 local atmospheric environment. *Build. Environ.* 41: 1352-1363.
- 808 [51]Cai, X., 2012. Effects of differential wall heating in street canyons on dispersion
809 and ventilation characteristics of a passive scalar. *Atmos. Environ.* 51: 268-277.

810 [52] Allegrini, J., Dorer, V., Carmeliet, J., 2014. Buoyant flows in street canyons:
811 Validation of CFD simulations with wind tunnel measurements. *Build. Environ.*
812 72: 63-74.

813 [53] Yang, X.Y., Li, Y.G., 2015. The impact of building density and building height
814 heterogeneity on average urban albedo and street surface temperature. *Build.*
815 *Environ.* 90: 146-156.

816 [54] Liu, J., Heidarinejad, M., Gracik, S., Srebric, J., 2015. The impact of exterior
817 surface convective heat transfer coefficients on the building energy consumption
818 in urban neighborhoods with different plan area densities. *Energy Build.* 86: 449–
819 463.

820 [55] Wang, X.X., Li, Y.G., 2016. Predicting urban heat island circulation using CFD.
821 *Build. Environ.* 99: 82-97.

822 [56] Fan, Y.F., Hunt, J.C.R., Li, Y.G., 2017. Buoyancy and turbulence-driven
823 atmospheric circulation over urban areas. *J. Environ. Sci.* 59: 63-71.

824 [57] Lin, Y., Chen, G., Chen, T., Luo, Z., Yuan, C., Gao, P., Hang, J., 2019. The
825 influence of advertisement boards, street and source layouts on CO dispersion
826 and building intake fraction in three-dimensional urban-like models. *Build.*
827 *Environ.* 150: 297-321.

828 [58] Habilomatis, G., Chaloulakou, A., 2015. A CFD modelling study in an urban
829 street canyon for ultrafine particles and population exposure: the intake fraction
830 approach. *Sci. Total Environ.* 530-531: 227-232.

- 831 [59]Baker, J., Walker, H.L., Cai, X.M., 2004. A study of the dispersion and transport
832 of reactive pollutants in and above street canyons - a large eddy simulation.
833 Atmos. Environ. 38: 6883-6892.
- 834 [60]Baik, J.-J., Kang, Y.-S., Kim, J.-J., 2007. Modeling reactive pollutant dispersion
835 in an urban street canyon. Atmos. Environ. 41: 934-949.
- 836 [61]Grawe, D., Cai, X.-M., Harrison, R.M., 2007. Large eddy simulation of shading
837 effects on NO₂ and O₃ concentrations within an idealised street canyon. Atmos.
838 Environ. 41: 7304-7314.
- 839 [62]Kang, Y.-S., Baik, J.J., Kim, J.J., 2008. Further studies of flow and reactive
840 pollutant dispersion in a street canyon with bottom heating. Atmos. Environ. 42:
841 4964-4975.
- 842 [63]Tong, N.Y.O., Leung, D.Y.C., 2012. Effects of building aspect ratio, diurnal
843 heating scenario, and wind speed on reactive pollutant dispersion in urban street
844 canyons. J. Environ. Sci.-China 24: 2091-2103.
- 845 [64]Zhong, J., Cai, X.M., Bloss, W.J., 2015. Modelling the dispersion and transport
846 of reactive pollutants in a deep urban street canyon: using large-eddy simulation.
847 Environ. Pollut. 200: 42-52.
- 848 [65]Kim, M.J., Park, R.J., Kim, J.J., 2012. Urban air quality modeling with full
849 O₃-NO_x-VOC chemistry: implications for O₃ and PM air quality in a street
850 canyon. Atmos. Environ. 47: 330-340.

851 [66]Park, S.J., Kim, J.J., Kim, M.J., Park, R.J., Cheong, H.-B., 2015. Characteristics
852 of flow and reactive pollutant dispersion in urban street canyons. *Bound. Layer*
853 *Meteorol.* 108: 20-31.

854 [67]Garmory, A., Kim, I.S., Britter, R.E., Mastorakos, E., 2009. Simulations of the
855 dispersion of reactive pollutants in a street canyon, considering different
856 chemical mechanisms and micromixing. *Atmos. Environ.* 43: 4670-4680.

857 [68]Kwak, K.H., Baik, J.J., 2012. A CFD modeling study of the impacts of NO_x and
858 VOC emissions on reactive pollutant dispersion in and above a street canyon.
859 *Atmos. Environ.* 46: 71-80.

860 [69]Kwak, K.H., Baik, J.J., Lee, K.Y., 2013. Dispersion and photochemical evolution
861 of reactive pollutants in street canyons. *Atmos. Environ.* 70: 98-107.

862 [70]Allan, M., Richardson, G.M., Jones-Otazo, H., 2008. Probability density
863 functions describing 24-hour inhalation rates for use in human health risk
864 assessments: an update and comparison. *Hum. Ecol. Risk. Assess.* 14: 372-391.

865 [71]Chau, C.K., Tu, E.Y., Chan, D.W.T., Burnett, C.J., 2002. Estimating the total
866 exposure to air pollutants for different population age groups in Hong Kong.
867 *Environ. Int.* 27: 617-630.

868 [72]Quang, T.N., He, C., Morawska, L., Knibbs, L.D., Falk, M., 2012. Vertical
869 particle concentration profiles around urban office buildings. *Atmos. Chem. Phys.*
870 12: 5017-5030.

- 871 [73]Tominaga, Y., Stathopoulos, T., 2013. CFD simulation of near-field pollutant
872 dispersion in the urban environment: A review of current modeling techniques.
873 Atmos. Environ. 79: 716-730.
- 874 [74]Zhang, Y.W., Gu, Z., Lee, S.C., Fu, T.M., Ho, K.F., 2011. Numerical simulation
875 and in situ investigation of fine particle dispersion in an actual deep street canyon
876 in Hong Kong. Indoor. Built. Environ. 20: 206-216.
- 877 [75]Salim, S.M., Buccolieri, R., Chan, A., Di Sabatino, S., 2011. Numerical
878 simulation of atmospheric pollutant dispersion in an urban street canyon:
879 comparison between RANS and LES. J. Wind Eng. Ind. Aerodyn. 99: 103-113.
- 880 [76]Ashie, Y., Kono, T., 2011. Urban-scale CFD analysis in support of a
881 climate-sensitive design for the Tokyo Bay area. Int. J. Climatol. 31: 174-188.
- 882 [77]Panagiotou, I., Neophytou, M.K.A., Hamlyn, D., Britter, R.E., 2013. City
883 breathability as quantified by the exchange velocity and its spatial variation in
884 real inhomogeneous urban geometries: An example from central London urban
885 area. Sci. Total Environ. 442: 466-477.
- 886 [78]Hang, J., Wang, Q., Chen, X.Y., Sandberg, M., Zhu, W., Buccolieri, R., Di
887 Sabatino, S., 2015. City breathability in medium density urban-like geometries
888 evaluated through the pollutant transport rate and the net escape velocity. Build.
889 Environ. 94: 166-182.

- 890 [79]Hang, J., Xian, Z., Wang, D., Mak, C. M., Wang, B., & Fan, Y., 2018. The
891 impacts of viaduct settings and street aspect ratios on personal intake fraction in
892 three-dimensional urban-like geometries. *Build. Environ.* 143: 138-162.
- 893 [80]ANSYS Inc, ANSYS FLUENT User's Guide, (Version 15.0).
- 894 [81]Seinfeld, J.H., Pandis, S.N., 1998. *Atmospheric Chemistry and Physics*.
895 Wiley-Interscience, New York.
- 896 [82]Lien, F.S., Yee, E., 2004. Numerical modeling of the turbulent flow developing
897 within and over a 3-D building array, part I: A high-resolution
898 Reynolds-averaged Navier-Stokers approach. *Bound-lay. Meteorol.* 112:
899 427-466.
- 900 [83]Santiago, J.L., Martilli, A., Martin, F., 2007. CFD simulation of airflow over a
901 regular array of cubes. Part I: three dimensional simulation of the flow and
902 validation with wind-tunnel measurements. *Bound-lay. Meteorol.* 122: 609-634.
- 903 [84]Tominaga, Y., Mochida, A., Yoshie, R., Kataoka, H., Nozu, T., Yoshikawa, M.,
904 Shirasawa T., 2008. AIJ guidelines for practical applications of CFD to pedestrian
905 wind environment around buildings. *J. Wind Eng. Ind. Aerodyn.* 96: 1749-1761.
- 906 [85]Franke, J., Hellsten, A., Schlünzen, H., Carissimo, B., 2007. Best practice
907 guideline for the CFD simulation of flows in the urban environment, in: *COST*
908 *Action 732*. pp. 1-52.
- 909 [86]Franke, J., Hellsten, A., Schlunzen, H., Carissimo, B., 2011. *The COST732 Best*

910 Practice Guideline for CFD simulation of flows in the urban environment a
 911 summary. *Int. J. Environ. Pollut.* 44: 419-427.

912 [87]Brown, M.J., Lawson, R.E., DeCroix, D.S., Lee, R. L., 2001. Comparison of
 913 centerline velocity measurements obtained around 2D and 3D building arrays in a
 914 wind tunnel. Report LA-UR-01-4138, Los Alamos National Laboratory, Los
 915 Alamos, pp.7.

916 [88]Blocken, B., Stathopoulos, T., Carmeliet, J., 2007. CFD simulation of the
 917 atmospheric boundary layer: wall function problems. *Atmos. Environ.* 41: 238–
 918 252.

919 [89]van Hooff, T., Blocken, B., 2013. CFD evaluation of natural ventilation of indoor
 920 environments by the concentration decay method: CO₂ gas dispersion from a
 921 semienclosed stadium. *Build. Environ.* 61: 1–17.

922 [90]Carslaw, D. C., 2005. Evidence of an increasing NO₂/NO_x emissions ratio from
 923 road traffic emissions. *Atmos. Environ.* 39(26): 4793-4802.

924 [91]Di Sabatino, S., Buccolieri, R., Olesen, H.R., Ketzler, M., Berkowicz, R., Franke,
 925 J., Schatzmann, M., Schlunzen, K.H., Leitl, B., Britter, R., Borrego, C., Costa,
 926 A.M., Trini Castelli, A., Reisin, T.G., Hellsten, A., Saloranta, J., Moussiopoulos,
 927 N., Barmpas, F., Brzozowski, K., Goricsan, I., Balczo, M., Bartzis, J.G.,
 928 Efthimiou, G., Santiago, J.L., Martilli, A., Piringer, M., Baumann-Stanzer, K.,
 929 Hirtl, M., Baklanov, A.A., Nuterman, R.B., Starchenko, A.V., 2011. COST 732
 930 in practice: the MUST model evaluation exercise. *Int. J. Env. Poll.* 44 (1/2/3/4).

[92]Chang, C. H., Meroney, R. N., 2001. Numerical and physical modeling of bluff body flow and dispersion in urban street canyons. *J. Wind Eng. Ind. Aerodyn.* 89 (14-15): 1325-1334.

[93]Irwin, J.S., 1979. A theoretical variation of the wind profile power-law exponent as a function of surface roughness and stability. *Atmos. Environ.* 13(1):191-194.

Figure list:

Fig.1 (a) The population census data of Hong Kong [4]; (b) Time activity patterns for each subgroup in four microenvironments [70].

Fig.2 (a) Idealized 3D urban district models ($H/W=1$, $\lambda_p=\lambda_f=0.25$); (b) Computational domains and boundary conditions for test cases; (c) The overhead and lateral views of mesh distribution.

Fig.3 Model setups of vehicular emission sources: (a) S3, (b) S10 and (c) Sm.

Fig.4 (a-b) The side and top views of measured points and model configurations in wind tunnel experiment [87]; (c) Computational domains and boundary conditions in CFD validation study; (d) The mesh arrangements in grid sensitivity test.

Fig.5 Results of grid independence test: (a) $\bar{u}(z)$, (b) $\bar{w}(z)$ at Point V1; Comparison of vertical profiles between wind tunnel data and CFD results: (c-e) $\bar{u}(z)$ at Points V1, V4 and V6, respectively; (f-g) $\bar{w}(z)$ and $k(z)$ at Point V1.

Fig.6 (a-b) The lateral and overhead views of experiment settings in concentration measurement [92]; (c) CFD setups in passive dispersion validation; (d-f) Vertical profiles of stream-wise velocity, turbulence kinetic energy and turbulent dissipation rate in domain inlet.

Fig.7 Comparison of K between wind tunnel data and CFD results applying standard $k-\varepsilon$ model: (a) on the leeward and windward walls; (b) on the central line of roof surface.

Fig.8 (a) Velocity distribution in the pedestrian level of $z=1.5\text{m}$; (b-c) Velocity magnitude and 2D streamlines for Street 3 (left) and 10 (right) in the plane of $y=30\text{m}$ and $z=1.5\text{m}$, respectively; (d) 3D streamlines in Street 3 and 10.

Fig.9 NO_2 concentration distribution between P-type (left or above) and R-type (right or below) cases: (a-b) in the plane of $y=30\text{m}$ with S3 and S10, respectively; (c-d) in the pedestrian level of $z=1.5\text{m}$ with S3 and S10, respectively; (e) in the pedestrian level of $z=1.5\text{m}$ with Sm.

Fig.10 (a-b) Photostationary state defect between S3 (left) and S10 (right) cases in $y=30\text{m}$ and $z=1.5\text{m}$, respectively.

Fig. 11 NO_2 concentration between P-type (left or above) and R-type (right or below) cases: (a-b) on the leeward and windward walls with S3 and S10, respectively; (c) on the entire building walls with Sm.

Fig.12 $\langle P_{iF} \rangle_B$ curves of NO and NO_2 in P-type and R-type cases with various source locations: (a) S3, (b) S10 and (c) Sm, respectively.

972 Fig. 13 $\langle P_{iF} \rangle_B$ curves of (a) NO₂ and (b) NO in P-type and R-type cases under four
973 O₃ background concentrations ([O₃]=1,20,40,100ppbv).

974 Fig. 14 $\langle P_{iF} \rangle_B$ curves of (a) NO₂ and (b) NO in P-type and R-type cases with three
975 kinds of NO-NO₂ emission ratios.

976

977 **Table list:**

978 Table 1 Time patterns and breathing rates in each subgroup for indoors at home ($j=1$)

979 Table 2 Summary of all test cases

980 Table 3 Comparison between wind tunnel experiment and CFD simulation

981 Table 4 $\langle P_{iF} \rangle_W$ (unit: ppm) at leeward and windward walls adjoining the target
982 street in S3 and S10 cases

983 Table 5 $\langle P_{iF} \rangle_B$ values and the exponential factor b in S3 and S10 cases

984